Journal of the Taiwan Institute of Chemical Engineers 179 (2026) 106434

Contents lists available at ScienceDirect

Journal of the Taiwan Institute of Chemical Engineers

journal homepage: www.journals.elsevier.com/journal-of-the-taiwan-institute-of-chemical-engineers

Metal-free β-ketoenamine-based conjugated microporous polymers: rational design of robust photocatalysts for efficient organic pollutant degradation

Mohamed Gamal Mohamed [a,b,1], Yang-Chin Kao [a,1], Shi-Quan Hong [a], Aya Farouk Farghal [a,b], Shiao-Wei Kuo [a,c,*]

[a] Department of Materials and Optoelectronic Science, Center of Crystal Research, National Sun Yat-Sen University, Kaohsiung 804, Taiwan
[b] Chemistry Department, Faculty of Science, Assiut University, Assiut, 71516, Egypt
[c] Department of Medicinal and Applied Chemistry, Kaohsiung Medical University, Kaohsiung 807, Taiwan

ARTICLE INFO

Keywords:
β-ketoenamine
Azobenzene
Dibenzothiophene dioxide
Conjugated microporous polymers
Photocatalytic dye degradation

ABSTRACT

Background: The rapid growth of industrialization has led to increased discharge of dye-laden wastewater, posing serious threats to aquatic ecosystems and water sustainability. Synthetic dyes like rhodamine B (RhB) and methylene blue (MB), known for their stable conjugated structures, resist biodegradation and persist in the environment. Their accumulation in water bodies harms aquatic life and can indirectly impact human health.
Methods: A series of metal-free β-ketoenamine-based conjugated microporous polymers (CMPs) was synthesized via Schiff-base polycondensation of an amine-terminated azobenzene monomer (AZO-2NH_2), 2,4,6-triformylphloroglucinol (TFP), and a diamino-substituted dibenzothiophene dioxide monomer (DBTD-2NH_2) under solvothermal conditions. By varying the molar feed ratio of AZO-2NH_2:TFP:DBTD-2NH_2 (2:2:1, 1.5:2:1.5, and 1:2:2), three CMP (AZO_2-TFP_2-$DBTD_1$, $AZO_{1.5}$-TFP_2-$DBTD_{1.5}$, AZO_1-TFP_2-$DBTD_2$) with tunable porosity, electronic structure, and morphology were obtained. Comprehensive spectroscopic characterization confirmed the complete formation of β-ketoenamine linkages, the successful incorporation of azo and DBTD motifs, and high chemical purity.
Significant Findings: Thermogravimetric analysis of AZO-TFP-DBTD CMPs revealed outstanding thermal stability (T_{d10} up to 461 °C, char yield up to 60.8 wt%). Nitrogen sorption studies demonstrated that our AZO-TFP-DBTD CMPs exhibited hierarchical micro- and mesoporosity, with Brunauer–Emmett–Teller (BET) surface areas ranging from 110 to 125 $m^2\ g^{-1}$ and dominant pore diameters of 1.7-2.0 nm. Ultraviolet photoelectron spectroscopy (UPS) and Tauc plot analyses of AZO-TFP-DBTD CMPs revealed a progressive deepening of the highest occupied molecular orbital (HOMO) level and a narrowing of the optical bandgaps (2.12-2.19 eV) as the DBTD content increased, thereby enhancing visible-light absorption. Photocatalytic evaluation using methylene blue (MB) and rhodamine B (RhB) as model dyes under visible irradiation revealed that AZO_1-TFP_2-$DBTD_2$ outperformed its counterparts, achieving greater than 98% degradation within 60 min and pseudo-first-order rate constants of up to 0.067 min^{-1}. Mechanistic studies identified singlet oxygen and photo-generated electrons as the primary reactive species. Recyclability tests of AZO_1-TFP_2-$DBTD_2$ confirmed excellent stability over three cycles with <10% loss in activity. This work highlights the effectiveness of molecular engineering and monomer stoichiometry in optimizing AZO-TFP-DBTD CMP photocatalysts for water remediation.

1. Introduction

With the rapid advancement of industrialization, dye-laden wastewater has become a growing concern, posing significant threats to aquatic resources and ecosystems [1–5]. Organic dye molecules such as rhodamine B (RhB) [6,7] and methylene blue (MB) [8,9] characterized by stable conjugated structures, are notoriously difficult to biodegrade and thus represent a persistent class of water contaminants [10–12].

* Corresponding author.
E-mail address: kuosw@faculty.nsysu.edu.tw (S.-W. Kuo).
[1] These two authors contributed equally.

https://doi.org/10.1016/j.jtice.2025.106434
Received 31 July 2025; Received in revised form 13 September 2025; Accepted 24 September 2025
Available online 29 September 2025

Traditional inorganic semiconductor photocatalysts, such as titanium dioxide (TiO_2) [13], zinc oxide (ZnO) [14,15], and graphitic carbon nitride (g-C_3N_4) [16], have demonstrated satisfactory photocatalytic activity and chemical stability under ultraviolet or visible light [17]. However, in practical applications, they exhibit several critical limitations: (1) a narrow absorption range within the visible spectrum, which restricts solar energy utilization [18]; (2) limited control over surface properties and microstructure, hindering efficient dye adsorption and catalyst-pollutant contact [19]; and (3) rapid recombination of photogenerated electron-hole pairs, resulting in low quantum efficiency and constrained photocatalytic degradation performance [20]. Consequently, the development of next-generation organic photocatalytic materials possessing broad-spectrum light absorption, tunable architectures, and enhanced charge separation has become a focal point in environmental remediation research [21].

Among emerging photocatalytic materials, conjugated microporous polymers (CMPs) have attracted widespread attention due to their extended π-conjugated networks [22–29], and highly tunable structures [30–34]. CMPs are synthesized via cross-linking of conjugated monomers, forming continuous π-conjugated frameworks that inherently exhibit strong visible-light absorption [23]. By rationally designing electron-donating and electron-withdrawing units, one can precisely tailor the bandgap of CMPs to respond to visible or even near-infrared light [35–37]. Moreover, the π-conjugated backbone of CMPs facilitates effective separation and rapid transport of photogenerated charges [38], thereby enhancing photocatalytic quantum efficiency. Intrinsically, CMPs often possess micro- or mesopores with specific surface areas ranging from several hundred to over 1,000 m^2/g, which provide abundant active sites for pollutant adsorption [39] and increase local concentration of target molecules, strengthening the coupling between adsorption and degradation processes. Notably, the incorporation of functional groups such as -NH_2 [40], -SO_3H [41], or azo (-N=N-) [42] moieties into the CMP network can further augment noncovalent interactions, π-π stacking, electrostatic attractions, or hydrogen bonding, between the polymer and dye molecules, thus improving both selectivity and degradation efficiency [43]. Compared to traditional inorganic semiconductors, CMPs offer unparalleled design freedom at the molecular level, enabling fine-tuning of surface properties, band structures, and catalytically active sites according to specific application requirements [44–46]. By integrating various photosensitive units, electron donors/acceptors, or metal coordination centers, the light absorption range of CMPs can be broadened and charge separation efficiency significantly improved [47].

Additionally, CMP frameworks typically rely on sturdy C=C or C=N bonds, endowing them with excellent chemical and thermal stability and making them suitable for both laboratory investigation and long-term cyclic use, key prerequisites for industrial scalability. In light of these advantages, the present study focuses on the intentional incorporation of azo groups (-N=N-) as crucial structural motifs within designed CMP materials [48]. Azo moieties possess extended conjugation and a high density of π electrons, which can engage in strong π-π stacking interactions with the aromatic rings of dye molecules, thereby boosting adsorption efficiency [49,50]. Moreover, azo groups themselves exhibit visible-light absorption and rapid electron-transfer characteristics, promoting efficient separation and transport of photoinduced charge carriers [51]. By ingeniously embedding azo units into the CMP framework, we anticipate synergistic enhancement of dye adsorption and photocatalytic degradation, offering novel design strategies for future organic photocatalysts [52]. RhB and MB were selected as representative aqueous dye pollutants. RhB, an xanthene-based cationic dye first synthesized by C. G. Grun in 1887, features a highly conjugated aromatic backbone and appears bright red to pink, with a maximum absorption wavelength near 554 nm. Its high fluorescence intensity and water solubility make it an ideal model compound for photocatalyst performance assessment. However, the presence of amino functional groups and aromatic rings renders RhB resistant to natural biodegradation [53], and its prolonged environmental persistence may pose mutagenic or carcinogenic risks to human health [54]. MB, a phenothiazine-based cationic dye first reported by Heinrich Caro in 1876, appears deep blue and finds extensive use in textile dyeing, medical diagnostics (cell and tissue staining) [55,56], and water quality assays [57]. With a maximum absorption wavelength around 665 nm, MB is similarly recalcitrant to environmental degradation and, upon long-term exposure, may cause skin irritation or central nervous system effects [58], making it a critical indicator of water pollution.

Advancing the photocatalytic efficacy of 2D CMPs necessitates the deliberate selection of robust covalent linkages and light-active monomeric units [59–62]. To this end, we explore the construction of new 2D CMP systems featuring extended π-conjugated networks to facilitate charge transport and light absorption [59,62]. A key component in this strategy is TFP, which undergoes condensation with arylamine derivatives to initially form enol–imine tautomers [63]. Subsequent isomerization leads to the generation of a radialene-like topology, distinguished by its electron-withdrawing nature and the reformation of carbonyl functionalities [64]. Further tautomeric shift to the *β*-keto-enamine configuration imparts enhanced thermodynamic stability, supported by intramolecular hydrogen bonding. This structural transformation not only reinforces the chemical durability of the framework but also augments its photophysical properties, positioning these CMPs as promising candidates for efficient visible-light photocatalysis [65]. Herein, three CMP networks were constructed through a Schiff base condensation reaction using AZO-2NH_2, TFP, and DBTD-2NH_2. The solvothermal synthesis was carried out using different molar combinations of the monomers (2:2:1, 1.5:2:1.5, and 1:2:2), leading to the formation of AZO_2-TFP_2-$DBTD_1$, $AZO_{1.5}$-TFP_2-$DBTD_{1.5}$, and AZO_1-TFP_2-$DBTD_2$, respectively. These AZO-TFP-DBTD CMP materials demonstrate adjustable textural properties, morphological diversity, and variable electronic configurations, highlighting the effectiveness of feed ratio tuning in structural and functional modulation. Photophysical properties of AZO-TFP-DBTD CMPs were probed by ultraviolet photoelectron spectroscopy (UPS) and ultraviolet–visible diffuse reflectance spectroscopy (UV–Vis DRS); respectively. To further elucidate the photocatalytic degradation mechanism of RhB, AZO_1-TFP_2-$DBTD_2$ CMP was selected as a model photocatalyst. Under visible light exposure, the material generates various reactive species—such as superoxide anions (O_2^-), photogenerated holes (h^+), singlet oxygen ($^1O_2$), and hydroxyl radicals (•OH)—which actively participate in breaking down organic pollutants during the photocatalytic process. Finally, the AZO-TFP-DBTD CMP materials were tested on simulated real-world dye effluent to examine their efficacy in complex aqueous matrices, thereby assessing their potential for industrial wastewater treatment.

2. Experimental section

2.1. Materials

2,5-Dibromoaniline (98%) and nitrosobenzene (98%) were obtained from MACKLIN and Combi-Blocks, respectively. Potassium carbonate (99%), anhydrous magnesium sulfate (99%), sodium azide, and anhydrous sodium carbonate (99.5%) were supplied by SHOWA. Dichloromethane (99.5%) and stannous chloride dihydrate ($SnCl_2{\cdot}2H_2O$, 98%) were purchased from Thermo Scientific, and dimethyl sulfoxide (DMSO) was acquired from Uniregion Bio-Tech. Tetrahydrofuran (THF, 99.9%), 1,4-dioxane (DO, 99.8%), 2-propanol (IPA, 99.9%), and hexane were obtained from Fisher Chemical, DUKSAN, and Merck. 4-(4,4,5,5-tetramethyl-1,3,2-dioxaborolan-2-yl)aniline (98%) was purchased from Sigma-Aldrich and tetrakis(triphenylphosphine)palladium(II) (98%) and dibenzo[*b,d*]thiophene 5,5-dioxide (DBTD) were obtained from Leyan. 1,3,5-Triformylphloroglucinol was supplied by Alfa Aesar, while *p*-benzoquinone (≥ 98%), ethylenediaminetetraacetic acid disodium salt dihydrate (EDTA-2Na, 99%), and acetic acid were procured from Alfa

Aesar and Honeywell, respectively.

2.2. Synthesis of (E)-1-(2,5-dibromophenyl)-2-phenyldiazene (AZO-2Br)

Nitrosobenzene (1.80 g, 16.8 mmol) and 2,5-dibromoaniline (2.40 g, 9.56 mmol) were introduced into a 50 mL round-bottom flask and dissolved in 15 mL of glacial acetic acid. The reaction mixture was heated to 60°C and stirred under a nitrogen atmosphere for 24 h to promote the formation of the corresponding azo intermediate. Upon completion, the reaction was neutralized by slowly adding solid sodium carbonate until bubbling stopped. The mixture was then extracted three times with dichloromethane (3×50 mL), and the combined organic layers were dried using anhydrous magnesium sulfate. Following filtration and evaporation of the solvent under reduced pressure, the obtained material was purified via silica gel column chromatography with hexane to afford an orange solid (1.53 g), corresponding to a 47% isolated yield. ^{1}H NMR (600 MHz, $CHCl_3$-*d*, δ, ppm): 7.99, 7.83-7.82, 7.63-7.60, 7.54-7.52, 7.45-7.44. ^{13}C NMR (600 MHz, $CHCl_3$-*d*, δ, ppm): 152.3, 150.0, 134.8, 134.4, 132.1, 129.2, 124.4, 123.6, 122.0, 121.0.

2.3. Synthesis of (E)-2′-(phenyldiazenyl)-[1,1′:4′,1′′-terphenyl]-4,4′′-diamine (AZO-2NH$_2$)

A Suzuki–Miyaura coupling reaction was carried out to synthesize the aminated AZO derivative. In a 150 mL round-bottom flask, AZO-2Br (1.10 g, 3.24 mmol), 4-(4,4,5,5-tetramethyl-1,3,2-dioxaborolan-2-yl) aniline (1.78 g, 8.12 mmol), $Pd(PPh_3)_2Cl_2$ (0.582 g, 0.82 mmol), and K_2CO_3 (1.29 g, 9.33 mmol) were combined in a solvent mixture consisting of deionized water (150 mL) and DO (60 mL). The heterogeneous mixture was heated to 100°C with vigorous stirring for 36 h to ensure complete conversion. Upon cooling to room temperature, an additional 150 mL of water was added, and the resulting biphasic suspension was extracted twice with dichloromethane (2×150 mL). The crude residue was purified by column chromatography on silica gel, eluting with hexane to afford a red-orange solid (0.76 g, 64% yield). This product was fully characterized by NMR and mass spectrometry and served as a key intermediate for subsequent polymerization studies. ^{1}H NMR (600 MHz, $CHCl_3$-*d*, δ): 7.85, 7.72, 7.69, 7.60-7.58, 7.54, 7.48, 7.35, 7.33, 6.79, 3.78; ^{13}C NMR (600 MHz, $CHCl_3$-*d*, δ, ppm): 152.9, 149.7, 146.0, 145.7,140.0, 138.9, 132.0, 130.75, 130.69, 130.6, 129.0, 128.8, 128.6, 128.0, 123.3, 115.4, 114.4,113.4.

2.4. Synthesis of 3,7-diaminodibenzo[b,d]thiophene 5,5-dioxide (DBTD-2NH$_2$)

DBTD (3.00 g, 13.87 mmol) was suspended in concentrated H_2SO_4, cooled to 0 °C, and nitrated with dropwise addition of concentrated HNO_3 over 30 min below 5 °C. After stirring at 25 °C for 24 h, the reaction was quenched in ice water, yielding the dinitro product (DBTD-2NO₂) as a precipitate.

The reaction mixture was then poured onto ice-water, causing precipitation of the dinitro derivative (DBTD-2NO$_2$). The pale-yellow solid was dried under reduced pressure to give DBTD-2NO$_2$ (3.30 g, 77% yield). In a reduction step, DBTD-2NO$_2$ (1.50 g, 4.89 mmol) was combined with $SnCl_2{\cdot}2H_2O$ (15.0 g, 66.47 mmol) in a mixture of acetic acid (50 mL) and concentrated HCl (20 mL). The mixture was maintained at 100 °C with continuous stirring for 24 h. Once cooled, it was poured into water to stop the reaction, and the pH was adjusted to neutrality using 40% aqueous NaOH. The precipitated diamine (DBTD-2NH$_2$) was isolated as a light-yellow solid (0.97 g, 81% yield). ^{1}H NMR (600 MHz, DMSO-*d*, δ): 7.50-7.48, 6.88-6.87, 6.80-6.78, 5.76; ^{13}C NMR (600 MHz, DMSO-*d*, δ): 149.2, 137.5, 121.4, 119.5, 118.5, 105.5.

2.5. Synthesis of AZO-TFP-DBTD CMPs

TFP, AZO-2NH$_2$, and DBTD-2NH$_2$ were added to a 25 mL Schlenk tube, followed by 1,4-dioxane (20 mL), mesitylene (10 mL), and 6 M acetic acid (1 mL) [different ratios as shown in **Table S1**]. The reaction mixture was heated to 120 °C under static conditions for 4 days. Upon completion, the mixture was gradually cooled to RT. The solid CMP was then collected by vacuum filtration and washed thoroughly with THF and DMF to remove unreacted monomers and oligomeric byproducts. The resulting solid was dried under vacuum to yield the final compounds.

3. Results and discussion

3.1. Synthesis and structural characterization of AZO-2NH$_2$ and DBTD-2NH$_2$ monomers

Fig. 1(a) depicts the synthetic route employed to obtain AZO-2NH$_2$, beginning with 2,5-dibromoaniline. Initially, 2,5-dibromoaniline underwent diazo coupling to yield a dibromo-terminated azo intermediate, designated AZO-2Br. Subsequently, a Suzuki–Miyaura coupling between AZO-2Br and 4-(4,4,5,5-tetramethyl-1,3,2-dioxaborolan-2-yl)aniline introduced an amine functionality, affording the target bifunctional monomer AZO-2NH$_2$ with terminal NH$_2$ groups. The attenuation and emergence of key vibrational bands in the FTIR spectra [Fig. 1(b)] corroborate this transformation. AZO-2Br exhibits characteristic sp^2 C-H stretching at 3058 cm^{-1} and a trans-N=N stretch at 1442 cm^{-1}. After Suzuki–Miyaura coupling, AZO-2NH$_2$ displays new N-H stretching bands at 3310 and 3200 cm^{-1} (asymmetric and symmetric modes, respectively), while the trans-N=N stretch shifts slightly to 1433 cm^{-1}, confirming successful incorporation of the aniline moiety. In the ^{1}H NMR spectrum [Fig. 1(c)], AZO-2Br shows aromatic proton resonances at 7.99, 7.83-7.82, 7.63-7.60, 7.54-7.52, and 7.45-7.44 ppm. Upon conversion to AZO-2NH$_2$, new signals corresponding to additional aromatic protons and the amine protons of the aniline unit emerge. In particular, a distinct resonance at 3.78 ppm is assigned to the -NH$_2$ protons. The aromatic region becomes more complex, with resonances observed at 7.85, 7.72, 7.69, 7.60-7.58, 7.54, 7.48, 7.35, 7.33, and 6.79 ppm, reflecting the expanded aromatic environment and confirming substitution at the dibromo sites. The ^{13}C NMR spectra [Fig. 1(d)] provide further evidence of structural evolution. For AZO-2Br, resonances at 152 and 150 ppm correspond to Ar-N=N carbons, while C-Br carbons appear at 122 and 121 ppm; additional aromatic carbons are observed between 134 and 123 ppm. After Suzuki-Miyaura coupling, the C-Br signals at 122 and 121 ppm diminish, and a new resonance at 145 ppm emerges, attributable to C-N carbons of the aniline units. The Ar-N=N carbons remain prominent at 153 and 149 ppm, and the aromatic carbon signals shift to a broader range of 140-113 ppm. Collectively, these spectroscopic changes confirm the successful conversion of AZO-2Br to AZO-2NH$_2$ and the successful installation of terminal amine groups.

Scheme S1 outlines the stepwise synthesis of the diamino-functionalized dibenzothiophene dioxide monomer (DBTD-2NH$_2$). In the first step, pristine DBTD was subjected to electrophilic nitration using a sulfuric acid and nitric acid mixture, affording the dinitro intermediate DBTD-2NO$_2$ in good yield. In the subsequent reduction step, treatment of DBTD-2NO$_2$ with stannous chloride in acidic acetic acid converted the nitro groups to primary amines, yielding the target bifunctional monomer DBTD-2NH$_2$ bearing two terminal -NH$_2$ groups. The successful installation of amine functionalities and preservation of the aromatic dibenzothiophene dioxide core were corroborated by FT-IR, ^{1}H NMR, and ^{13}C NMR spectroscopy. As shown in **Fig. S1**, the FT-IR spectrum of DBTD-2NH$_2$ features two intense bands at 3474 and 3372 cm^{-1}, assigned to the asymmetric and symmetric stretching vibrations of the primary amine N-H bonds, respectively. A medium-intensity band centered at 1610 cm^{-1} arises from N-H bending coupled with aromatic C=C stretching, while additional modes between 1500 and 1450 cm^{-1} correspond to aromatic C=C vibrations. The C-N stretching of the conjugated amine appears as a distinct band in the 1320–1250 cm^{-1} region. In the ^{1}H NMR spectrum [**Fig. S2**], DBTD-

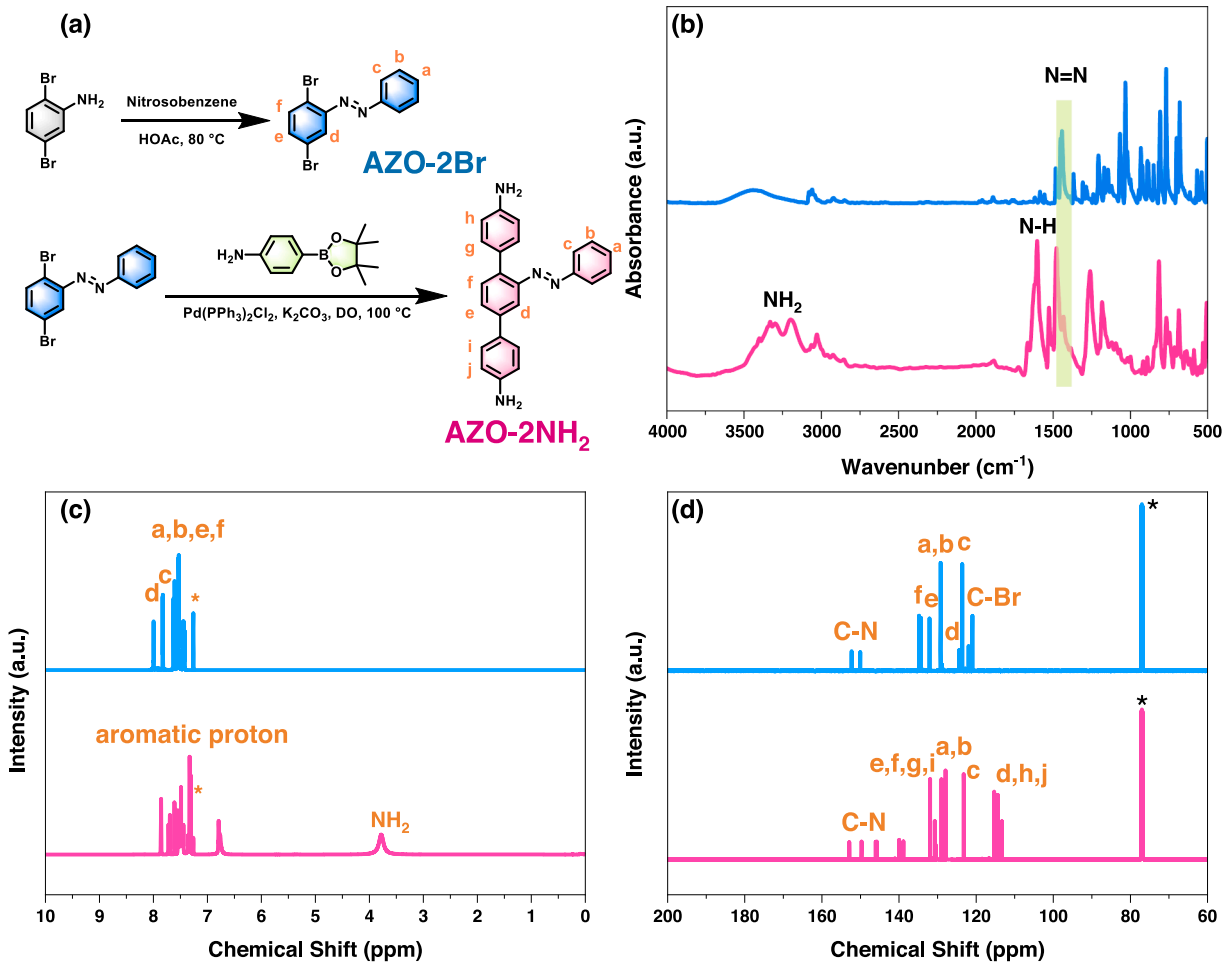

Fig. 1. (a) Synthesis route of AZO-2Br and AZO-2NH_2 and their corresponding (b) FTIR spectrum, (c) ^{1}H NMR, and (d) ^{13}C NMR spectrum (* is the peak for $CHCl_3$-*d*).

2NH_2 displays characteristic aromatic proton resonances at 7.50-7.48, 6.88-6.87, and 6.80-6.78 ppm, alongside a signal at 5.76 ppm attributable to the -NH_2 protons. The ^{13}C NMR spectrum [**Fig. S3**] further confirms the aromatic framework, revealing carbon resonances between 149 and 105 ppm consistent with the dibenzothiophene dioxide skeleton. Collectively, these spectral data validate the synthesis of DBTD-2NH_2 and its suitability as a diamine group for subsequent CMP construction.

3.2. *Synthesis and structural characterization of AZO-TFP-DBTD CMPs*

Fig. 2(a) shows the three monomeric building blocks employed in the preparation of our AZO-TFP-DBTD-based CMPs: the amine-functionalized azobenzene derivative (AZO-2NH_2), 2,4,6-triformylphloroglucinol (TFP), and the diamino-substituted dibenzothiophene dioxide (DBTD-2NH_2). By varying the stoichiometric ratios of AZO-2NH_2 to TFP to DBTD-2NH_2 (2:2:1, 1.5:2:1.5, and 1:2:2), we obtained three distinct CMP networks, denoted AZO_2-TFP_2-$DBTD_1$, $AZO_{1.5}$-TFP_2-$DBTD_{1.5}$, and AZO_1-TFP_2-$DBTD_2$, respectively. The FTIR spectra of all three AZO-TFP-DBTD [Fig. 2(b)] display nearly identical absorption patterns, indicating a common core framework. Broad O-H stretching bands appear between 3694 and 3260 cm^{-1}, while aromatic C=C vibrations are observed at 1600-1500 cm^{-1}. The azo N=N stretching modes manifest at 1454–1447 cm^{-1} [66,67]. Crucially, no bands corresponding to primary amine (-NH_2) or aldehyde (-CHO) functionalities remain, confirming quantitative Schiff-base condensation. Solid-state ^{13}C NMR spectroscopy [Fig. 2(c)] further verifies the successful formation of the azo-based CMP frameworks and highlights subtle variations arising from different monomer feed ratios.

In all three networks, intense resonances between 107 and 138 ppm can be ascribed to conjugated aromatic carbons, including the C-S moieties of the DBTD units. In each case, a signal at approximately 156-157 ppm corresponds to the aromatic C-OH carbon of the phloroglucinol-derived linkage, confirming complete Schiff-base condensation. The appearance of a downfield resonance between 184 and 187 ppm indicates keto-enamine tautomerization of the *β*-ketoenamine linkages, with the precise chemical shift increasing slightly as the DBTD content rises (184 ppm for AZO_2-TFP_2-$DBTD_1$; 186 ppm for $AZO_{1.5}$-TFP_2-$DBTD_{1.5}$; 187 ppm for AZO_1-TFP_2-$DBTD_2$). Additional resonances at 178-179 ppm are attributed to the C=C-NH carbons, while signals at 147-148 ppm correspond to imine (C=N) carbons.

Thermogravimetric analysis [**Fig. S4**] demonstrates that all three AZO-TFP-DBTD exhibit excellent thermal stability, with the temperature at 10% weight loss (T_{d10}) and residual char yields varying according to monomer composition. Specifically, AZO_2-TFP_2-$DBTD_1$ decomposes at T_{d10} = 424°C and retains 55.9 wt% char yield, while $AZO_{1.5}$-TFP_2-$DBTD_{1.5}$ displays enhanced stability with T_{d10} = 460°C and a char yield of 52.0 wt%. Notably, increasing the DBTD content further to yield AZO_1-TFP_2-$DBTD_2$ raises T_{d10} marginally to 461°C and boosts the residual char to 60.8 wt%. These results indicate that a higher proportion of the thermally robust dibenzothiophene dioxide unit contributes to a more stable crosslinked framework, underscoring the crucial role of monomer feed ratio in tuning the thermal properties of CMP networks. High-resolution X-ray photoelectron spectroscopy (XPS) was employed to elucidate the elemental composition and chemical environments within the three AZO-TFP-DBTD [Fig. 2(d)].

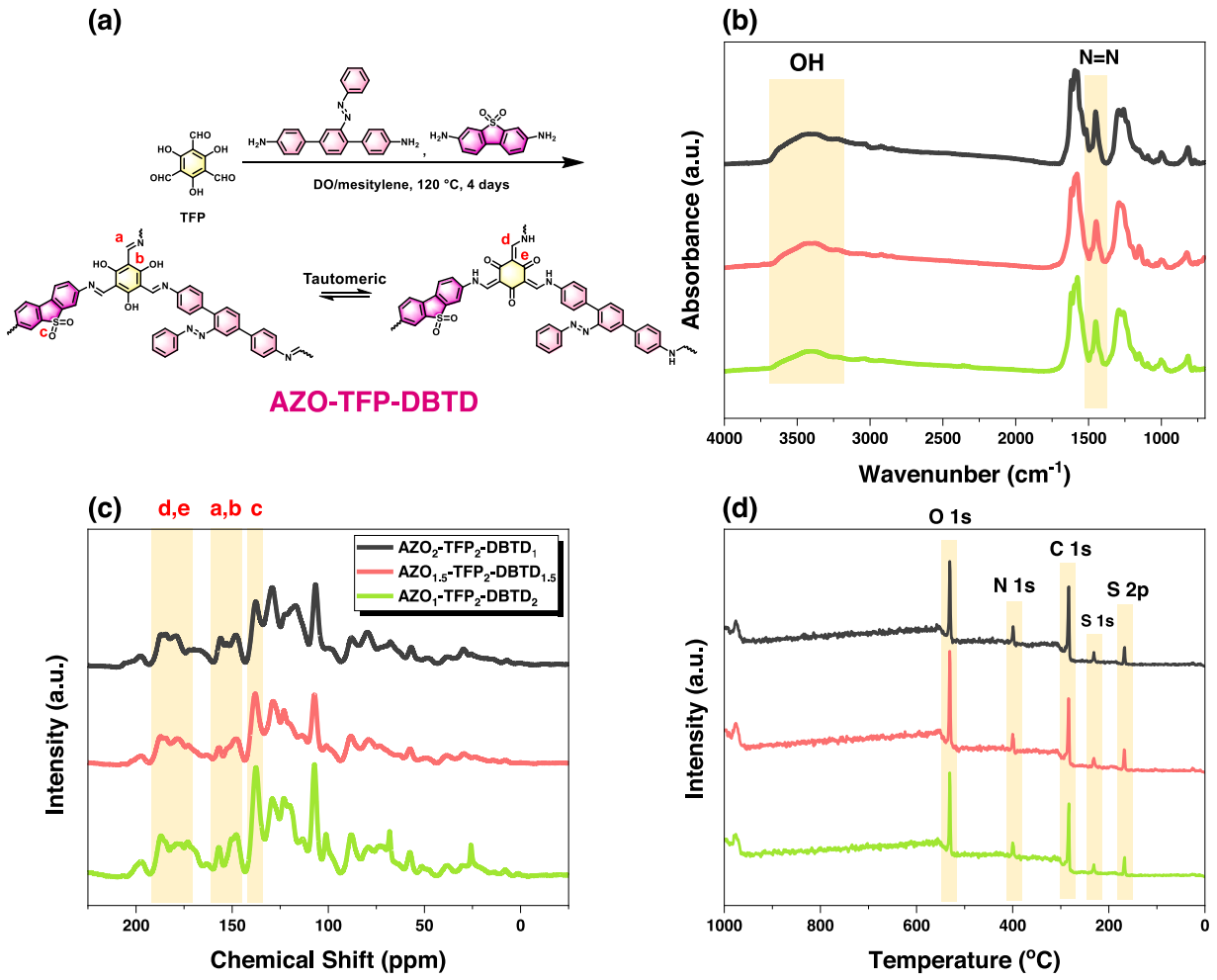

Fig. 2. (a) Synthesis route of AZO-TFP-DBTD-based CMPs and the corresponding (b) FTIR spectrum, (c) solid-state ^{13}C NMR spectrum, and (d) XPS spectra.

In each sample, survey spectra confirm the presence of carbon, nitrogen, oxygen, and sulfur. The high-resolution C 1s region displays four deconvoluted components: a peak at 284 eV assigned to C=C bonds, peaks at 284.5-284.7 eV corresponding to C-S thioether linkages, a component at 285.1 eV attributable to C-N bonds from amine and imine functionalities, and a higher-energy feature at 286.1-286.2 eV arising from carbonyl (C=O) groups [Fig. 3(a)**, Fig. S5(a) and Fig. S6(a)**] [65]. In the N 1s region, two distinct peaks at 398.6-398.7 eV and 400.4-400.5 eV are observed, which we ascribe to amine nitrogen (C-N) and azo nitrogen (N=N), respectively, verifying successful incorporation of both functionalities [Fig. 3(b)**, Fig. S5(b), and Fig. S6(b)**] [65]. The O 1s spectra for all AZO-TFP-DBTD exhibit three components: a dominant band at 530.9 eV for carbonyl oxygen, a shoulder at 530.0 eV assigned to oxidized sulfur (S=O), and a higher-energy feature near 532.3-532.6 eV due to adsorbed water [Fig. 3(c)**, Fig. S5(c) and Fig. S6(c)**] [65]. Finally, the S 1s region appears at 231 eV and the S 2p region reveals the characteristic doublet of covalently bound sulfur at 167.1-167.2 eV (S $2p_{1/2}$) and ~168.3-168.5 eV (S $2p_{3/2}$), along with a minor high-binding-energy component indicative of oxidized sulfur species [Fig. 3 (d)**, Fig. S5(d) and Fig. S6(d)**] [65].

Across the three CMPs, AZO_2-TFP_2-$DBTD_1$, $AZO_{1.5}$-TFP_2-$DBTD_{1.5}$, and AZO_1-TFP_2-$DBTD_2$, these spectral features remain consistent, demonstrating that variations in monomer feed ratio do not alter the fundamental chemical composition, but rather modulate the relative intensities of these key signals in accordance with the sulfur content of AZO-TFP-DBTD-based CMPs. In addition, elemental analysis was performed to confirm the chemical composition and purity of the three AZO-TFP-DBTD CMPs networks [**Table S2**]. For AZO_2-TFP_2-$DBTD_1$, the measured contents were C 67.78 wt%, N 9.91 wt%, O 15.10 wt%, and S 1.69 wt%. In the case of $AZO_{1.5}$-TFP_2-$DBTD_{1.5}$, the CMP contained C 64.02 wt%, N 9.34 wt%, O 19.87 wt%, and S 5.27 wt%. Finally, AZO_1-TFP_2-$DBTD_2$ exhibited C 57.48 wt%, N 8.04 wt%, O 21.74 wt%, and S 6.46 wt%. The systematic decrease in carbon and nitrogen alongside increasing oxygen and sulfur with higher DBTD loading aligns precisely with the intended monomer feed ratios and confirms that the dibenzothiophene dioxide units have been successfully incorporated into the CMP structures.

Nitrogen adsorption-desorption measurements [Fig. 4(a-c)] reveal that all three AZO-TFP-DBTD-based CMPs display type IV isotherms with pronounced hysteresis loops, indicating a hierarchical microporous-mesoporous architecture. Brunauer–Emmett–Teller (BET) analysis yields specific surface areas of 126, 118, and 110 $m^2\ g^{-1}$ for AZO_2-TFP_2-$DBTD_1$, $AZO_{1.5}$-TFP_2-$DBTD_{1.5}$, and AZO_1-TFP_2-$DBTD_2$, respectively. Pore size distributions and total pore volumes determined by non-local density functional theory (NLDFT; **Table S2**) confirm dominant micropore diameters of approximately 1.7 nm for AZO_2-TFP_2-$DBTD_1$, 2.0 nm for $AZO_{1.5}$-TFP_2-$DBTD_{1.5}$, and 1.8 nm for AZO_1-TFP_2-$DBTD_2$, underscoring the microporous nature of these CMPs [Fig. 4]. Scanning electron microscopy (SEM) further highlights the impact of monomer feed ratio on morphology: AZO_2-TFP_2-$DBTD_1$ exhibits a loosely packed, highly porous texture consistent with its elevated surface area [Fig. 5(a)]; $AZO_{1.5}$-TFP_2-$DBTD_{1.5}$ presents denser, larger aggregates [Fig. 5(f)]; and AZO_1-TFP_2-$DBTD_2$ forms uniformly spherical particles, likely reflecting balanced nucleation and growth under its specific monomer composition [Fig. 5(k)]. Collectively, these results demonstrate that tuning the AZO:TFP:DBTD stoichiometry provides an

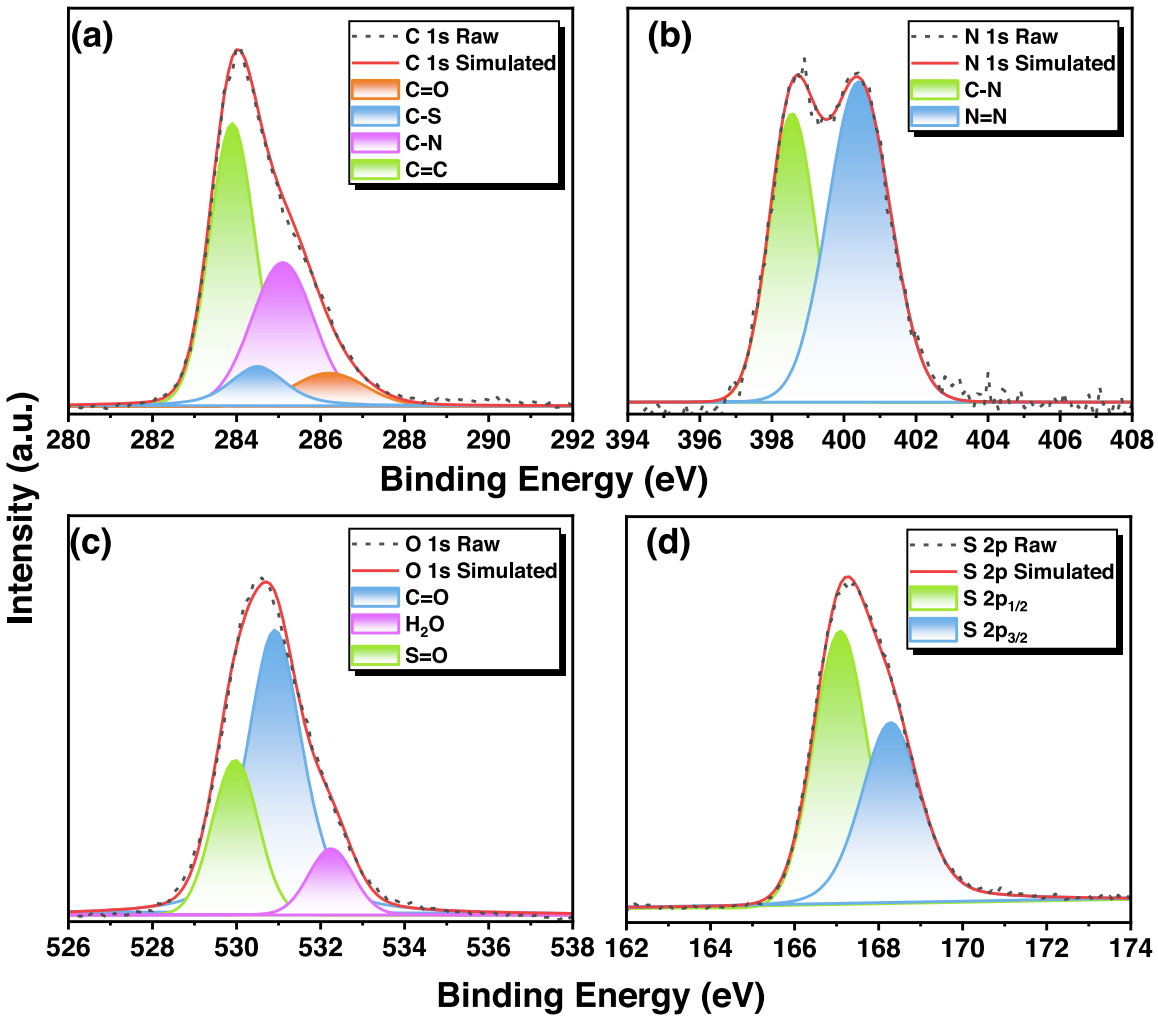

Fig. 3. Deconvolution spectra of the XPS (a) carbon, (b) nitrogen, (c) oxygen, and (d) sulfur for AZO_2-TFP_2-$DBTD_1$ CMP framework.

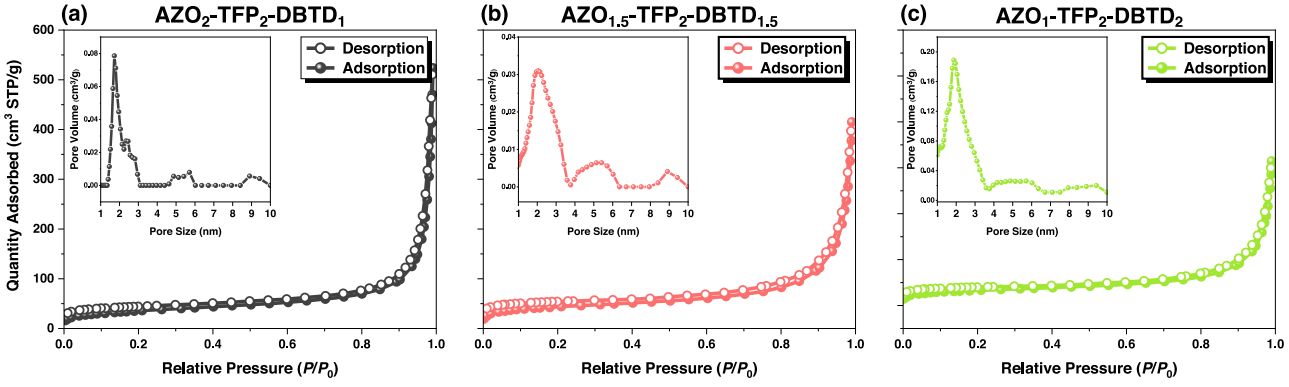

Fig. 4. (a-c) N_2 adsorption/desorption isotherms of (a) AZO_2-TFP_2-$DBTD_1$, (b) $AZO_{1.5}$-TFP_2-$DBTD_{1.5}$, and (c) AZO_1-TFP_2-$DBTD_2$ [**Inset Fig. 4(a-c):** pore size distribution of AZO_2-TFP_2-$DBTD_1$, $AZO_{1.5}$-TFP_2-$DBTD_{1.5}$, and AZO_1-TFP_2-$DBTD_2$].

effective handle for modulating both the porous structure and particle morphology of CMP networks. Furthermore, scanning electron microscopy coupled with energy-dispersive X-ray spectroscopy (SEM-EDS) confirmed the presence of the anticipated elements—C, N, O, and S within the AZO_2-TFP_2-$DBTD_1$, $AZO_{1.5}$-TFP_2-$DBTD_{1.5}$, and AZO_1-TFP_2-$DBTD_2$ frameworks. The elemental composition obtained from SEM-EDS analysis is consistent with the structural information derived from the XPS patterns shown in Fig. 2(d), thereby supporting the successful incorporation of the targeted building blocks into the frameworks. Moreover, XRD analysis revealed that the AZO_2-TFP_2-$DBTD_1$, $AZO_{1.5}$-TFP_2-$DBTD_{1.5}$, and AZO_1-TFP_2-$DBTD_2$ frameworks exhibit amorphous structures, as evidenced by the absence of sharp diffraction peaks and the presence of broad, diffuse halos in their patterns [**Fig. S7**], while TEM images further confirm their disordered morphologies. [**Fig. S8**].

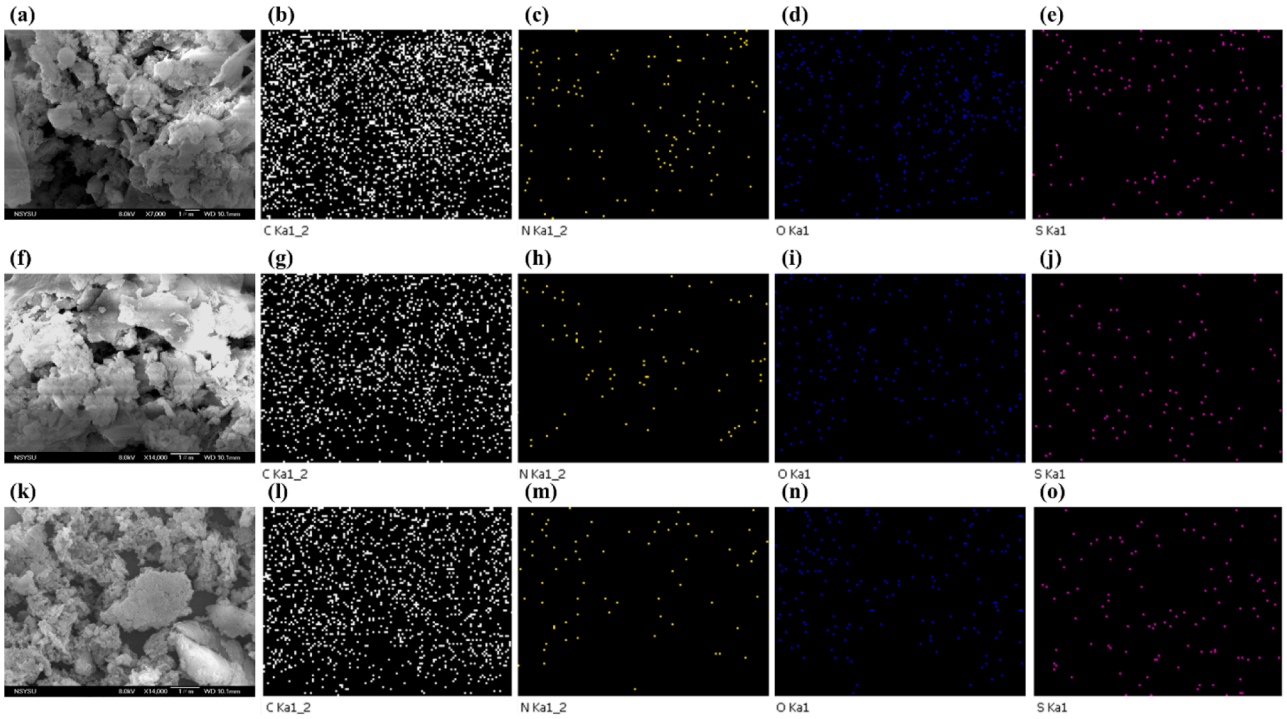

Fig. 5. (a, f, k) SEM images and (b, c, d, e, g, h, I, j, l, m, n, o) SEM-EDS images of (a-e) AZO_2-TFP_2-$DBTD_1$, (f-j) $AZO_{1.5}$-TFP_2-$DBTD_{1.5}$, and (k-o) AZO_1-TFP_2-$DBTD_2$.

3.3. Photophysical properties of AZO_2-TFP_2-$DBTD_1$, $AZO_{1.5}$-TFP_2-$DBTD_{1.5}$, and AZO_1-TFP_2-$DBTD_2$

To ensure efficient photocatalytic activity, photocatalysts must exhibit appropriate optical band gaps and favorable photophysical properties. Accordingly, UPS and UV–Vis DRS analyses were employed to investigate these properties in AZO-TFP-DBTD CMPs. UPS was utilized to evaluate the HOMO energy levels of the AZO-TFP-DBTD CMPs. As illustrated in Fig. 6(a)-6(c)), the corresponding UPS spectra were analyzed to extract the secondary electron cutoff (E_{cutoff}) and the valence band onset (E_{onset}) through linear extrapolation methods [68]. The work function φ was calculated for AZO_2-TFP_2-$DBTD_1$,

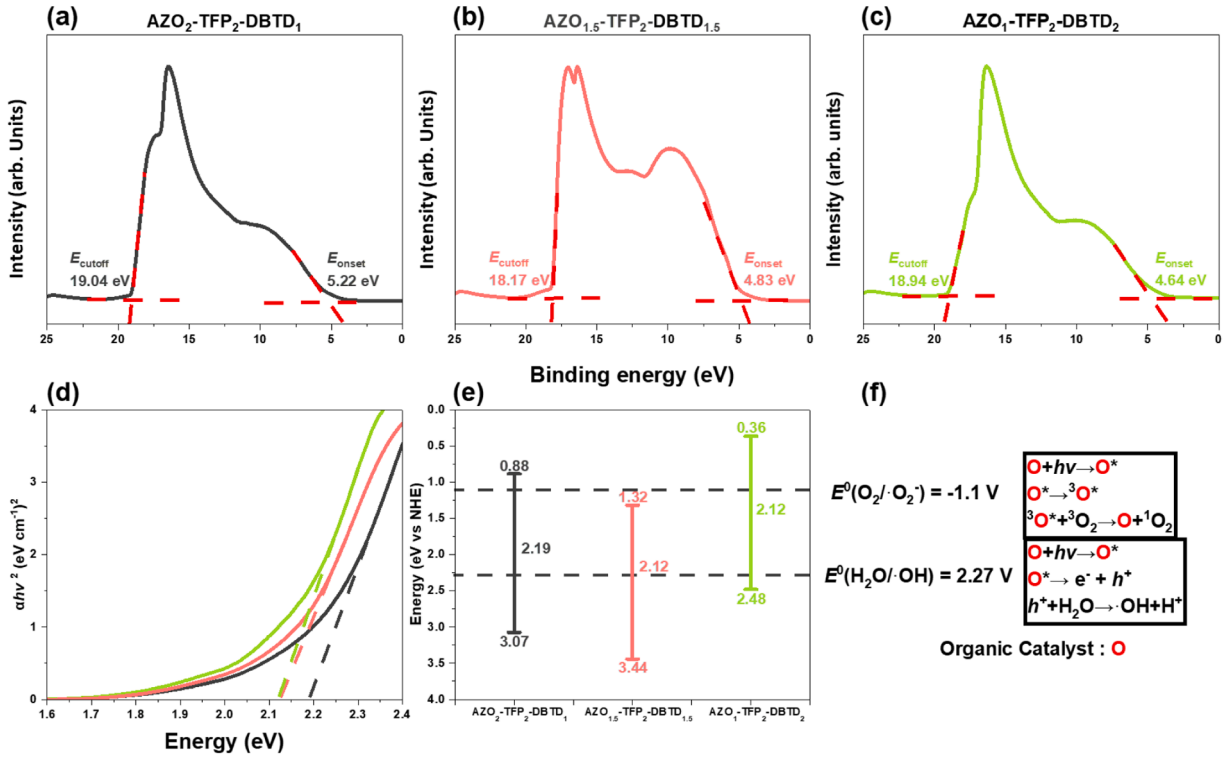

Fig. 6. UPS spectra of (a) AZO_2-TFP_2-$DBTD_1$, (b) $AZO_{1.5}$-TFP_2-$DBTD_{1.5}$, and (c) AZO_1-TFP_2-$DBTD_2$; (d) Tauc plot, (e) energy level diagram, and (f) possible photocatalytic reaction mechanism of Azo-based CMPs.

$AZO_{1.5}$-TFP_2-$DBTD_{1.5}$, and AZO_1-TFP_2-$DBTD_2$; respectively.

$\varphi = h\nu - Ecutoff$ (with $h\nu = 21.22$ eV for He I excitation)

Based on E_{cutoff} and E_{onset} from the UPS spectra, the HOMO energy levels of the AZO-TFP-DBTD CMPs. *HOMO* levels were calculated from $-HOMO = \varphi + E_{onset}$ to be 3.07 eV for the black sample (AZO_2-TFP_2-$DBTD_1$), 3.44 eV for the red sample ($AZO_{1.5}$-TFP_2-$DBTD_{1.5}$), and 2.48 eV for the green sample (AZO_1-TFP_2-$DBTD_2$). These values reflect a progressive deepening of the HOMO level with increasing DBTD content, indicating enhanced electron-withdrawing character and greater oxidative potential. The optical band gaps of the AZO-TFP-DBTD CMPs were determined using Tauc plots, derived from the Tauc–Davis–Mott relationship: $(\alpha h\nu)^2 = K(hc/\lambda - E_g)$ [69,70]. In this method, a plot of $(\alpha hc/\lambda)^2$ versus photon energy (hc/λ) was constructed, and the linear portion of the curve was extrapolated to the x-axis to estimate the band gap energy, as illustrated in Fig. 6(d). Here, α represents the absorption coefficient, hc/λ corresponds to the energy of incident photons, K is a material-dependent constant, and E_g denotes the band gap. Based on this analysis, the band gap energies for AZO_2-TFP_2-$DBTD_1$, $AZO_{1.5}$-TFP_2-$DBTD_{1.5}$, and AZO_1-TFP_2-$DBTD_2$ were calculated to be 2.19 eV, 2.12 eV, and 2.12 eV, respectively, as shown in Fig. 6(d). By integrating the band gap values obtained from the Tauc plots with the HOMO energy levels, the complete band structure diagrams were constructed, as presented in Fig. 6(e). Overall, the narrower band gap of $AZO_{1.5}$-TFP_2-$DBTD_{1.5}$ and AZO_1-TFP_2-$DBTD_2$, along with their enhanced absorption in the visible light region and more favorable HOMO energy alignment, collectively underscore their superior photophysical characteristics. These attributes make $AZO_{1.5}$-TFP_2-$DBTD_{1.5}$ and AZO_1-TFP_2-$DBTD_2$ more promising candidates for photocatalytic applications compared to AZO_2-TFP_2-$DBTD_1$, which exhibits comparatively weaker optical and electronic performance. The proposed photocatalytic mechanism involves the generation of reactive oxygen species (ROS), which play a critical role in the degradation of organic pollutants [Fig. 6(f)]. Under visible-light irradiation, if the conduction band (CB) potential of the photocatalyst is more negative than the reduction potential of $O_2/\bullet O_2^-$ (−1.1 V vs. NHE), photogenerated electrons can effectively reduce molecular oxygen to form superoxide radicals ($\bullet O_2^-$). Simultaneously, if the valence band (VB) potential is more positive than the oxidation potential of $OH^-/\bullet OH$ (+2.27 V vs. NHE), photogenerated holes can oxidize hydroxide ions or water molecules to generate highly reactive hydroxyl radicals (•OH). Both $\bullet O_2^-$ and •OH are powerful oxidizing agents that contribute significantly to the breakdown of dye molecules and other organic contaminants in the photocatalytic process.

3.4. Photocatalytic dye degradation efficiency of AZO_2-TFP_2-$DBTD_1$, $AZO_{1.5}$-TFP_2-$DBTD_{1.5}$, and AZO_1-TFP_2-$DBTD_2$ toward methylene blue (MB) and rhodamine B (RhB)

Motivated by the exceptional surface areas, good porosity, excellent

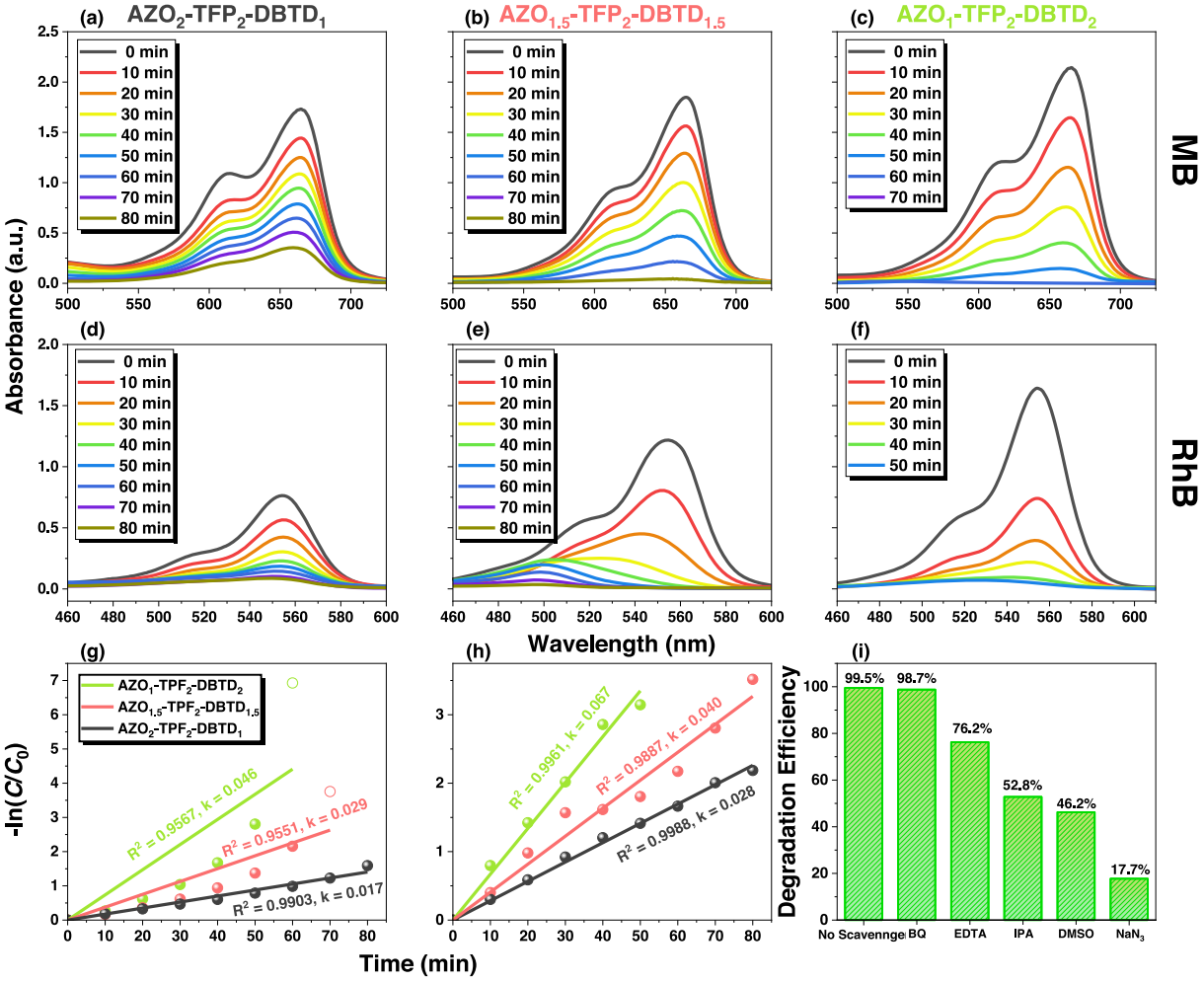

Fig. 7. UV-Vis spectra of degradation for (a-c) MB and (d-f) RhB with (a, d) AZO_2-TFP_2-$DBTD_1$, (b, e) $AZO_{1.5}$-TFP_2-$DBTD_{1.5}$ and (c, f) AZO_1-TFP_2-$DBTD_2$, (g, h) $\ln(C_0/C)$ versus irradiation duration plot of (g) MB and (h) RhB degradation and (i) the photodegradation efficiency after adding various scavengers into AZO_1-TFP_2-$DBTD_2$/RhB solution.

dispersibility, and favorable photophysical properties of AZO_2-TFP_2-$DBTD_1$, $AZO_{1.5}$-TFP_2-$DBTD_{1.5}$, and AZO_1-TFP_2-$DBTD_2$-based CMPs, we systematically investigated their photocatalytic performance in the degradation of hazardous MB and RhB dyes. Control experiments confirmed that, in the absence of photocatalysts or under dark conditions, both MB and RhB exhibit negligible degradation, highlighting the critical role of the CMPs in driving the photodegradation process. Subsequently, 5 mg of each CMP [AZO_2-TFP_2-$DBTD_1$, $AZO_{1.5}$-TFP_2-$DBTD_{1.5}$, and AZO_1-TFP_2-$DBTD_2$] was introduced into 10 mL of 50 ppm MB and RhB solutions to evaluate their photocatalytic degradation capabilities at different times under visible light irradiation, as illustrated in Fig. 7(a)–7(f). At the initial stage (time zero) under visible light irradiation, the AZO-TFP-DBTD CMP in the presence of MB displayed two distinct absorption peaks at 613 nm and 665 nm. In contrast, when exposed to RhB, the same CMP exhibited a broad characteristic band centered around 518 nm, along with an additional absorption peak at 555 nm. As observed in Fig. 7(a)–7(c), the photocatalytic degradation performance of the AZO-TFP-DBTD CMPs toward MB varied significantly with their composition. After 80 min of visible light irradiation, AZO_2-TFP_2-$DBTD_1$ exhibited only limited photocatalytic activity, indicating a relatively low efficiency in degrading MB. This suggests that a higher ratio of the AZO component may not favor optimal photocatalytic performance, possibly due to reduced electron transfer efficiency or fewer active sites. In contrast, $AZO_{1.5}$-TFP_2-$DBTD_{1.5}$ demonstrated improved photocatalytic degradation after 80 min, indicating that a balanced ratio between AZO and DBTD components enhances photocatalytic efficiency. Most notably, AZO_1-TFP_2-$DBTD_2$ showed the fastest degradation of MB, achieving significant dye removal within just 70 min. This superior performance is likely attributed to the higher DBTD content, which may facilitate more effective charge separation and light absorption, ultimately accelerating the degradation process. These findings highlight the critical role of monomer composition in tuning the photocatalytic activity of CMPs. Similarly, the photocatalytic degradation performance of AZO-TFP-DBTD CMPs toward RhB is illustrated in Fig. 7(d)–7(f). After 80 min of visible light exposure, both AZO_2-TFP_2-$DBTD_1$ and $AZO_{1.5}$-TFP_2-$DBTD_{1.5}$ exhibited minimal degradation of RhB, indicating limited photocatalytic efficiency. In sharp contrast, AZO_1-TFP_2-$DBTD_2$ exhibited a markedly enhanced photocatalytic response, achieving substantial RhB degradation within 50 min. This superior performance can be attributed to the increased DBTD content, which likely promotes better light absorption, more efficient charge carrier mobility, and a higher density of active sites. As illustrated in **Fig. S9**, AZO_1-TFP_2-$DBTD_2$ demonstrated outstanding photocatalytic efficiency toward MB, achieving approximately 99.5% degradation within 60 mins. In comparison, AZO_2-TFP_2-$DBTD_1$ and $AZO_{1.5}$-TFP_2-$DBTD_{1.5}$ achieved lower degradation rates of 81.3% and 93.3%, respectively, under the same conditions.

Similarly, **Fig. S10** reveals that AZO_1-TFP_2-$DBTD_2$ also exhibited excellent performance in degrading RhB, reaching 98.5% degradation after 60 min. This is slightly higher than the efficiencies observed for AZO_2-TFP_2-$DBTD_1$ (95.4%) and $AZO_{1.5}$-TFP_2-$DBTD_{1.5}$ (94.5%). These results consistently demonstrate that increasing the DBTD content enhances the photocatalytic capabilities of the CMPs across both dye systems. The photocatalytic degradation process followed pseudo-first-order kinetics, as determined through kinetic modeling. $\ln(C_0'/C_t) = kt$, where C_0' is the pollutant concentration at the onset of light irradiation in 0 min, C_t is the concentration at time t, and k is the rate constant. From the linear pseudo-first-order plots [Figs. 7(f) and 7(g)], AZO_1-TFP_2-$DBTD_2$ was identified as the most active photocatalyst, achieving rate constants (k) of 0.046 min^{-1} for MB and 0.067 min^{-1} for RhB, with corresponding correlation coefficients of 0.9567 and 0.9961. Liquid chromatography–mass spectrometry (LC-MS) analysis was conducted on the reaction mixtures at different time intervals under visible light irradiation to monitor the degradation pathways of MB and RhB catalyzed by AZO_1-TFP_2-$DBTD_2$. The LC-MS spectra revealed a stepwise breakdown of MB, starting from the parent ion at m/z 284. Progressive fragmentation led to the formation of intermediate species with m/z values of 270, 256, 228, 173, 166, 142, 110, 72, and 64, indicating systematic demethylation, ring cleavage, and molecular scission processes [**Scheme S2, Fig. S11**]. Similarly, the degradation of RhB began with the molecular ion at m/z 443, followed by the appearance of a series of lower-mass fragments at m/z 415, 387, 359, 331, 317, 273, 73, and 60. These findings confirm that both dyes underwent multi-step oxidative degradation, ultimately forming smaller, less toxic molecules under the influence of the AZO_1-TFP_2-$DBTD_2$ photocatalyst [**Scheme S3, Fig. S12**]. The photocatalytic degradation of RhB is known to be significantly influenced by the presence of reactive oxygen species, including superoxide radicals ($\bullet O_2^-$), photo-generated holes (h^+), hydroxyl radicals ($\bullet OH$), and singlet oxygen ($^1O_2$) [69,70]. To gain deeper insight into the underlying degradation mechanism facilitated by AZO_1-TFP_2-$DBTD_2$, a series of radical scavenger experiments [benzoquinone (BQ), EDTA-Na, isopropanol (IPA), DMSO (e^-), and NaN_3] were conducted [Fig. 7(i)] [71]. The addition of NaN_3, known to quench singlet oxygen ($^1O_2$) and photogenerated electrons, caused a dramatic reduction in degradation efficiency, from 99.5% to 17.7%. This significant suppression highlights the crucial role of $^1O_2$ and electrons in the degradation process. IPA, a scavenger for hydroxyl radicals ($\bullet OH$), reduced the degradation efficiency to 52.8%, while EDTA, a hole (h^+) scavenger, decreased it to 76.2%. DMSO, as an electron scavenger, further lowered the efficiency to 46.2%. In contrast, BQ, which targets superoxide radicals ($\bullet O_2^-$), had a minimal impact on the reaction, slightly decreasing the degradation to 98.7%.

These results collectively suggest that singlet oxygen and photogenerated electrons are the primary reactive species responsible for RhB decomposition, followed by contributions from $\bullet OH$ and h^+. The photocatalytic stability and reusability of the AZO-TFP-DBTD CMPs were evaluated through three consecutive degradation cycles of MB and RhB under visible-light irradiation. As depicted in Fig. 8(a), the MB degradation efficiency of AZO_2-TFP_2-$DBTD_1$ exhibited only a slight decrease from 98% in the first cycle to 91% after the third. Similarly, $AZO_{1.5}$-TFP_2-$DBTD_{1.5}$ showed a reduction from 99% to 93%, while AZO_1-TFP_2-$DBTD_2$ declined modestly from 98% to 94%. In the case of RhB degradation [Fig. 8(b)], the photocatalytic activity of AZO_2-TFP_2-$DBTD_1$ dropped slightly from 89% to 83% over three cycles. Meanwhile, $AZO_{1.5}$-TFP_2-$DBTD_{1.5}$ and AZO_1-TFP_2-$DBTD_2$ maintained higher stability, with only minor decreases from 98% to 94% and 99% to 95%, respectively. These results demonstrate the excellent photocatalytic durability and recyclability of the AZO-TFP-DBTD CMPs materials, particularly AZO_1-TFP_2-$DBTD_2$, which retained high degradation efficiency with minimal loss over repeated use.

4. Conclusions

We have demonstrated a versatile synthetic strategy for constructing azo-functionalized donor–π–acceptor CMPs through the rational combination of an azobenzene (AZO), a phloroglucinol-derived linker (TFP), and a dibenzothiophene dioxide (DBTD). By adjusting the relative proportions of these monomers, we achieved systematic control over the CMP's porosity, electronic energy levels, and light-harvesting capabilities. Spectroscopic and thermal analyses confirmed robust β-ketoenamine frameworks with high chemical purity and exceptional thermal stability. Importantly, increasing the DBTD content led to deeper HOMO levels, narrower bandgaps, and enhanced visible-light absorption, which translated directly into superior photocatalytic performance. Photocatalytic performance was assessed using MB and RhB as representative dyes under visible light exposure. Among the tested materials, AZO_1-TFP_2-$DBTD_2$ demonstrated superior activity, achieving over 98% dye degradation within 60 mins and exhibiting pseudo-first-order kinetics with rate constants reaching 0.067 min^{-1}. Mechanistic investigations revealed that singlet oxygen and photo-induced electrons played dominant roles in the degradation process. Furthermore, recyclability experiments showed that the AZO_1-TFP_2-$DBTD_2$ photocatalyst

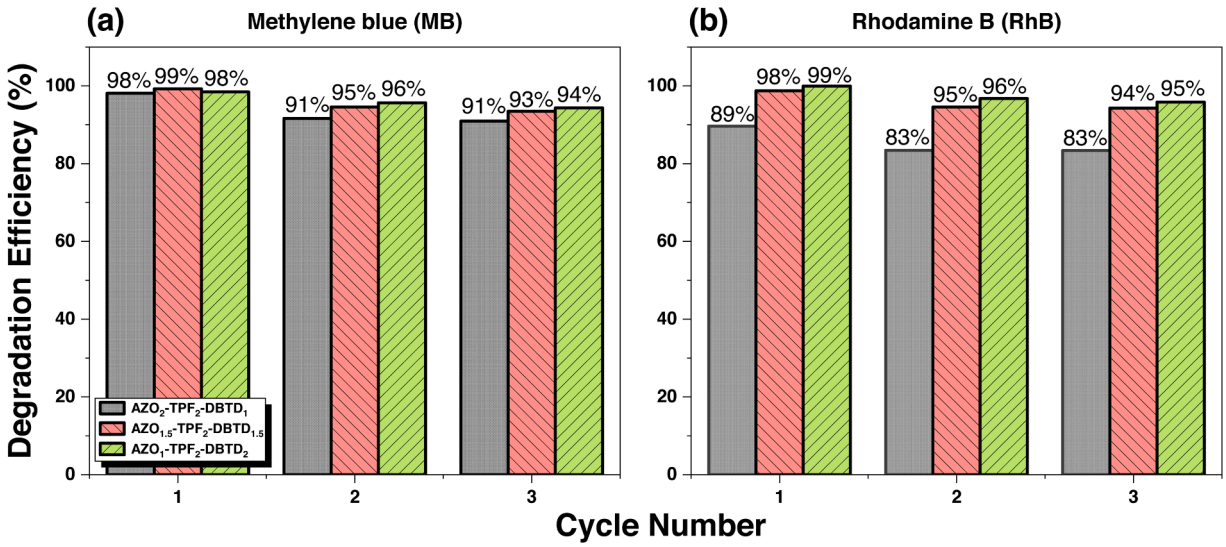

Fig. 8. The cyclic photodegradation of (a) MB and (b) RhB solution with AZO-TFP-DBTD-based CMPs.

maintained excellent stability, with less than 10% reduction in activity after three successive cycles.

CRediT authorship contribution statement

Mohamed Gamal Mohamed: Writing – review & editing, Writing – original draft, Supervision, Methodology, Investigation, Formal analysis, Conceptualization. **Yang-Chin Kao:** Formal analysis, Data curation, Conceptualization. **Shi-Quan Hong:** Formal analysis. **Aya Farouk Farghal:** Data curation. **Shiao-Wei Kuo:** Supervision, Resources.

Declaration of competing interest

The authors declare that they have no known competing financial interests or personal relationships that could have appeared to influence the work reported in this paper.

Acknowledgments

This study was supported financially by the National Science and Technology Council, Taiwan, under contracts NSTC 114-2223-E-110-001- and 113-2221-E-110-012-MY3. The authors thank the staff at National Sun Yat-sen University for their assistance with the TEM (ID: EM022600) experiments.

Supplementary materials

Supplementary material associated with this article can be found, in the online version, at doi:10.1016/j.jtice.2025.106434.

References

[1] Abadi PGS, Irani M, Rad LR. Mechanisms of the removal of the metal ions, dyes, and drugs from wastewaters by the electrospun nanofiber membranes. J Taiwan Inst Chem Eng 2023;143:104625. https://doi.org/10.1016/j.jtice.2022.104625.

[2] Liu AW, Liu JX, Chen MY, Tseng CH, Wen YJ, Chen YC, Kuo CY. Electrospun silk fibroin nanofibers with fluorescent carbon quantum dots for efficient photodegradation of environmental pollutants. J Taiwan Inst Chem Eng 2025:106351. https://doi.org/10.1016/j.jtice.2025.106351.

[3] Mohamed MG, Elewa AM, Chen NP, Mohammed AAK, Kuo SW. Construction of malononitrile-functionalized conjugated microporous polymers as adsorbents for effective adsorption of Rhodamine B and density functional theory perspective. Colloids Surf A: Physicochem Eng Asp 2025;721:137214. https://doi.org/10.1016/j.colsurfa.2025.137214.

[4] Hsiao CW, Elewa AM, Mohamed MG, Kotp MG, Chou MMC, Kuo SW. Designing strategically functionalized hybrid porous polymers with octavinylsilsesquioxane/dibenzo[g,p]chrysene/benzo[c]-1,2,5-thiadiazole units for rapid removal of Rhodamine B dye from water. Colloids Surf A: Physicochem Eng Asp 2024;699:134658. https://doi.org/10.1016/j.colsurfa.2024.134658.

[5] Hsiao CW, Elewa AM, Mohamed MG, Kuo SW. Highly stable hybrid porous polymers containing polyhedral oligomeric silsesquioxane (POSS)/Dibenzo[g,p]chrysene and Dibenzo[b,d]thiophene units for efficient Rhodamine B dye removal. Sep Purif Technol 2024;332:125771. https://doi.org/10.1016/j.seppur.2023.125771.

[6] Kao YC, Mohamed MG, Chen YH, Ejaz M, Kuo SW. Synergistic engineering of pyrene–thiazolothiazole-based donor–π–acceptor conjugated microporous polymers with heteroatom embedding for efficient visible-light photocatalyst for organic dye degradation. ACS Polym Au 2025. https://doi.org/10.1021/acspolymersau.5c00083.

[7] Kotp MG, Mohamed MG, Wang PT, Hassan AE, Elewa AM, Kuo SW. Unlocking the potential of n,n,n',n'-Tetraphenylbenzidine based on conjugated microporous polymers for rhodamine b adsorption: a synergistic experimental and density functional theory perspective. ACS Polym Au 2025;5:379–93. https://doi.org/10.1021/acspolymersau.5c00025.

[8] Hussain J, Hussain A, Lin KS, Hassan N, Abbas A, Badshah SM, Mdlovu NV, Rehman W. Degradation of methylene blue under visible-light with copper-doped cobalt oxide nanoparticles. J Taiwan Inst Chem Eng 2024;165:105819. https://doi.org/10.1016/j.jtice.2024.105819.

[9] Ashamary F, Neba PC, Harivarsha S, Raji A, Annamalai P, Mohamed MG, Kalambate P, Muthirulan P, Kuo SW, Manoj D. In situ synthesis of 3D ZIF-8 on 2D MXene nanosheets for efficient photocatalytic degradation of methylene blue (MB). Mater Adv 2025;6:4660–71. https://doi.org/10.1039/D5MA00340G.

[10] Jaihindh DP, Lin YF, Tseng LH, Krisbiantoro PA, Wu KCW, Shukla K, Sone M, Chang TFM, Chen CY. Heterogeneous Z-scheme CuO/ZnO aerogel photocatalyst for photocatalytic degradation of organic dye. J Taiwan Inst Chem Eng 2025;175:106281. https://doi.org/10.1016/j.jtice.2025.106281.

[11] Sharma J, Sharma S, Soni V. Classification and impact of synthetic textile dyes on Aquatic Flora: a review. Reg Stud Mar Sci 2021;45:101802. https://doi.org/10.1016/j.rsma.2021.101802.

[12] Ejaz M, Mohamed MG, Kotp MG, Elewa AM, Kuo SW. Triphenylamine-linked triazine (D-A) units based Hypercrosslinked porous polymer: rapid adsorption and enhanced photodegradation of organic dyes from water. Colloids Surf A: Physicochem Eng Asp 2025;722:137239. https://doi.org/10.1016/j.colsurfa.2025.137239.

[13] Armaković SJ, Savanović MM, Armaković S. Titanium dioxide as the most used photocatalyst for water purification: an overview. Catalysts 2022;13:26. https://doi.org/10.3390/catal13010026.

[14] Chang JS, Strunk J, Chong MN, Poh PE, Ocon JD. Multi-dimensional zinc oxide (ZnO) nanoarchitectures as efficient photocatalysts: what is the fundamental factor that determines photoactivity in ZnO? J Hazard Mater 2020;381:120958. https://doi.org/10.1016/j.jhazmat.2019.120958.

[15] Bica BO, de Melo JVS. Concrete blocks nano-modified with zinc oxide (ZnO) for photocatalytic paving: performance comparison with titanium dioxide (TiO_2). Constr Build Mater 2020;252:119120. https://doi.org/10.1016/j.conbuildmat.2020.119120.

[16] Zhang C, Li Y, Shuai D, Shen Y, Xiong W, Wang L. Graphitic carbon nitride (g-C_3N_4)-based photocatalysts for water disinfection and microbial control: a review. Chemosphere 2019;214:462–79. https://doi.org/10.1016/j.chemosphere.2018.09.137.

[17] Nemiwal M, Zhang TC, Kumar D. Recent progress in g-C_3N_4, TiO_2 and ZnO based photocatalysts for dye degradation: Strategies to improve photocatalytic activity. Sci Total Env 2021;767:144896. https://doi.org/10.1016/j.scitotenv.2020.144896.

[18] Wang X, Wang F, Sang Y, Liu H. Full-spectrum solar-light-activated photocatalysts for light–chemical energy conversion. Adv Energy Mater 2017;7:1700473. https://doi.org/10.1002/aenm.201700473.
[19] Rytwo G, Klein T, Margalit S, Mor O, Naftali A, Daskal G. A continuous-flow device for photocatalytic degradation and full mineralization of priority pollutants in water. Desal Water Treat 2016;57:16424–34. https://doi.org/10.1080/19443994.2015.1077749.
[20] Jiang L, Yuan X, Zeng G, Wu Z, Liang J, Chen X, Leng L, Wang H, Wang H. Metal-free efficient photocatalyst for stable visible-light photocatalytic degradation of refractory pollutant. Appl Catal B: Env 2018;221:715–25. https://doi.org/10.1016/j.apcatb.2017.09.059.
[21] Ahamd I, Li G, Abduljawad MM, Alfaifi MQ, Alrashed YI, Albaqi FM. Shedding light on covalent organic framework photocatalysts: concept, design strategies, and applications-a review. Green Chem 2025;27:7042–81. https://doi.org/10.1039/d5gc01774b.
[22] Mohamed MG, EL-Mahdy AFM, Kotp MG, Kuo SW. Advances in porous organic polymers: syntheses, structures, and diverse applications. Mater Adv 2022;3:707–33. https://doi.org/10.1039/D1MA00771H.
[23] Yang Y, Li X, Zhang Y, Zhang L, Zang L, Xu Z, Sun L. Synthesis of flower-like covalent organic frameworks for photocatalytic selective oxidation of sulfide. J Taiwan Inst Chem Eng 2024;164:105680. https://doi.org/10.1016/j.jtice.2024.105680.
[24] Chang SY, Elewa AM, Mohamed MG, Mekhemer IMA, Samy MM, Zhang K, Chou HH, Kuo SW. Rational design and synthesis of bifunctional Dibenzo [g, p] chrysene-based conjugated microporous polymers for energy storage and visible light-driven photocatalytic hydrogen evolution. Mater Today Chem 2023;33:101680. https://doi.org/10.1016/j.mtchem.2023.101680.
[25] Mohamed MG, Chen CC, Ibrahim M, Mousa AO, Elsayed MH, Ye Y, Kuo SW. Tetraphenylanthraquinone and Dihydroxybenzene-Tethered Conjugated Microporous Polymer for Enhanced CO_2 Uptake and Supercapacitive Energy Storage. JACS Au 2024;4:3593–605. https://doi.org/10.1021/jacsau.4c0053.7.
[26] Samy MM, Mohamed MG, Sharma SU, Chaganti SV, Lee JT, Kuo SW. An Ultrastable Tetrabenzonaphthalene-Linked conjugated microporous polymer functioning as a high-performance electrode for supercapacitors. J Taiwan Inst Chem Eng 2024;158:104750. https://doi.org/10.1016/j.jtice.2023.104750.
[27] Mohamed MG, Atayde Jr EC, Matsagar BM, Na J, Yamauchi Y, Wu KCW, Kuo SW. Construction hierarchically mesoporous/microporous materials based on block copolymer and covalent organic framework. J Taiwan Inst Chem Eng 2020;112:180–92. https://doi.org/10.1016/j.jtice.2020.06.013.
[28] Mohamed MG, Sharma SU, Wang PT, Ibrahim M, Lin MH, Liu CL, Ejaz M, Yen HJ, Kuo SW. Construction of fully π-conjugated, diyne-linked conjugated microporous polymers based on Tetraphenylethene and dibenzo [g, p] chrysene units for energy storage. Polym Chem 2024;15:2827–39. https://doi.org/10.1039/D4PY00421C.
[29] Mohamed MG, Chen TC, Kuo SW. Solid-state chemical transformations to enhance gas capture in benzoxazine-linked conjugated microporous polymers. Macromolecules 2021;54:5866–77. https://doi.org/10.1021/acs.macromol.1c00736.
[30] Mohamed MG, Halder B, Singh PN, Mohammed AAK, Elumalai P, Kuo SW. Molecular engineering and synergistic redox-active hexaazatrinaphthalene and pyrene-based conjugated microporous polymers for superior faradaic supercapacitor energy storage. Chem Eng J 2025;520:165892. https://doi.org/10.1016/j.cej.2025.165892.
[31] Mohamed MG, Chang WC, Kuo SW. Crown ether-and benzoxazine-linked porous organic polymers displaying enhanced metal ion and CO_2 capture through solid-state chemical transformation. Macromolecules 2022;55:7879–92. https://doi.org/10.1021/acs.macromol.2c01216.
[32] Mohamed MG, Mansoure TH, Samy MM, Takashi Y, Mohammed AA, Ahamad T, Alshehri SM, Kim J, Matsagar BM, Wu KCW. Ultrastable conjugated microporous polymers containing benzobisthiadiazole and pyrene building blocks for energy storage applications. Molecules 2022;27:2025. https://doi.org/10.3390/molecules27062025.
[33] Samy MM, Mekhemer IMA, Mohamed MG, Elsayed MM, Lin KH, Chen YK, Wu TL, Chou HH, Kuo SW. Conjugated microporous polymers incorporating Thiazolo [5,4-d] thiazole moieties for Sunlight-Driven hydrogen production from water. Chem Eng J 2022;446:137158. https://doi.org/10.1016/j.cej.2022.137158.
[34] Zhang W, Luo X, Tang H, Tang Z, Huang F, Wan Q, Yu G, Yang H. Structural regulation of sulfone-decorated conjugated polymers for boosting photocatalysis. J Mater Chem A 2025;13:4746–93. https://doi.org/10.1039/d4ta07264b.
[35] Qian Z, Zhang KAI. Recent Advances of Conjugated Microporous Polymers in Visible Light–Promoted Chemical Transformations. Sol RRL 2020;5:2000489. https://doi.org/10.1002/solr.202000489.
[36] Dou L, Liu Y, Hong Z, Li G, Yang Y. Low-Bandgap Near-IR Conjugated Polymers/Molecules for Organic Electronics. Chem Rev 2015;115:12633–65. https://doi.org/10.1021/acs.chemrev.5b00165.
[37] Zheng L, Lu Z, Yang H, Zhao R, Wang M, Hou L, Xiao L. Electron transport by intramolecular cascaded π-conjugation channels of D-A two-dimensional conjugated microporous polymer mediate photo-induced RCMP. Polymer 2023;282:126163. https://doi.org/10.1016/j.polymer.2023.126163.
[38] Tang M, Wan J, Wang Y, Ye G, Yan Z, Ma Y, Sun J. Insights into molecular imprinting polydopamine in-situ activating peroxydisulfate for targeted removal of refractory organic pollutants: overlooked N site. Appl Catal B: Env 2023;334:122852. https://doi.org/10.1016/j.apcatb.2023.122852.
[39] Patra K, Pal H. Recent advances in Porous Organic Polymers (POPs): the emerging sorbent materials with promises towards toxic and radionuclides metal ions separations. Mater Today Sustain 2024;27:100799. https://doi.org/10.1016/j.mtsust.2024.100799.
[40] Zang Y, Yu Y, Chen Y, Fan M, Wang J, Liu J, Xu L, Jia H, Dong S. Synthesis of conjugated microporous polymers rich in sulfonic acid groups for the highly efficient adsorption of Cs^+. Chem Eng J 2024;484:149709. https://doi.org/10.1016/j.cej.2024.149709.
[41] Ma W, Zhang C, Gao X, Shu C, Yan C, Wang F, Chen Y, Zeng JH, Jiang J-X. Structure evolution of azo-fused conjugated microporous polymers for high performance lithium-ion batteries anodes. J Power Sources 2020;453:227868. https://doi.org/10.1016/j.jpowsour.2020.227868.
[42] Feng G, Sun Y, Yuan J, Qian J, Siam N, Fa D, Ji W, Zhang E, Shen Y, Yan J, Lei S, Hu W. A CMP-based [FeFe]-hydrogenase dual-functional biomimetic system for photocatalytic hydrogen evolution coupled with degradation of tetracycline. Appl Catal B: Env 2024;340:123200. https://doi.org/10.1016/j.apcatb.2023.123200.
[43] Chen L, Yang Y, Jiang D. CMPs as scaffolds for constructing porous catalytic frameworks: a built-in heterogeneous catalyst with high activity and selectivity based on nanoporous metalloporphyrin polymers. J Am Chem Soc 2010;132:9138–43. https://doi.org/10.1021/ja1028556.
[44] Mousa AO, Mohamed MG, Lin ZI, Chuang CH, Chen CK, Kuo SW. Construction of cationic conjugated microporous polymers containing pyrene units through post-cationic modification for enhanced antibacterial performance. J Taiwan Inst Chem Eng 2024;157:105448. https://doi.org/10.1016/j.jtice.2024.105448.
[45] Mohamed MG, Li MS, Elewa AM, Kuo SW. Construction and multifunctional of hypercrosslinked porous organic polymers containing ferrocene unit for high-performance iodine adsorption and supercapacitor. J Taiwan Inst Chem Eng 2023;150:105045. https://doi.org/10.1016/j.jtice.2023.105045.
[46] Zhang H, Li S, Qian Z, Yin J, Wei W, Zhao Y, Zhang KAI. Efficient photocatalytic chloride dehalogenation by planar conjugated microporous polymers with enhanced charge separation and transport. Mater Adv 2024;5:2169–74. https://doi.org/10.1039/d3ma00994g.
[47] Qin L, Ma C, Zhang J, Zhou T. Structural motifs in covalent organic frameworks for photocatalysis. Adv Funct Mater 2024;34:2401562. https://doi.org/10.1002/adfm.202401562.
[48] Sagadevan S, Rahman MZ, Leonard E, Losic D, Hessel V. Sensor to electronics applications of graphene oxide through AZO grafting. Nanomaterials 2023;13:846. https://doi.org/10.3390/nano13050846.
[49] Cheng Y, Chen Y, He M, Zhou N, Meng X, Dai Z, Xiong Y. Photo-tunable ultrafast removal of organic dyes by azobenzene and phosphonium functionalized porous organic polymers. Sep Purif Technol 2024;335:126119. https://doi.org/10.1016/j.seppur.2023.126119.
[50] Gao M, Kwaria D, Norikane Y, Yue Y. Visible-light-switchable azobenzenes: Molecular design, supramolecular systems, and applications. Nat Sci 2023;3:e220020. https://doi.org/10.1002/ntls.20220020.
[51] Zhou Z, Chen IC, Rehman LM, Aboalsaud AM, Shinde DB, Cao L, Zhang Y, Lai Z. Conjugated microporous polymer membranes for light-gated ion transport. Sci Adv 2022;8:eabo2929. https://doi.org/10.1126/sciadv.abo2929.
[52] Khan I, Saeed K, Zekker I, Zhang B, Hendi AH, Ahmad A, Ahmad S, Zada N, Ahmad H, Shah LA, Shah T, Khan I. Review on methylene blue: its properties, uses, toxicity and photodegradation. Water 2022;14:242. https://doi.org/10.3390/w14020242.
[53] Mohod AV, Momotko M, Shah NS, Marchel M, Imran M, Kong L, Boczkaj G. Degradation of rhodamine dyes by Advanced Oxidation Processes (AOPS)–focus on cavitation and photocatalysis-a critical review. Water Resour Ind 2023;30:100220. https://doi.org/10.1016/j.wri.2023.100220.
[54] Cwalinski T, Polom W, Marano L, Roviello G, D'Angelo A, Cwalina N, Matuszewski M, Roviello F, Jaskiewicz J, Polom K. Methylene blue-current knowledge, fluorescent properties, and its future use. J Clin Med 2020;9:3538. https://doi.org/10.3390/jcm9113538.
[55] Gupta M, Shrivastava K, Raghuvanshi V, Ojha S, Gupta A, Sasidhar S. Application of in vivo stain of methylene blue as a diagnostic aid in the early detection and screening of oral cancerous and precancerous lesions. J Oral Maxillofac Pathol 2019;23:304. https://doi.org/10.4103/jomfp.JOMFP_242_17.
[56] Ben Said M, Bousselmi L, Ghrabi A. Monitoring of methylene blue monomers and dimers to control the bacterialogical water quality including application to photocatalysis. Env Sci Pollut Res Int 2021;28:15819–27. https://doi.org/10.1007/s11356-020-11767-z.
[57] Oladoye PO, Ajiboye TO, Omotola EO, Oyewola OJ. Methylene blue dye: toxicity and potential elimination technology from wastewater. Results Eng 2022;16:100678. https://doi.org/10.1016/j.rineng.2022.100678.
[58] Luo S, Zeng Z, Zeng G, Liu Z, Xiao R, Xu P, Wang H, Huang D, Liu Y, Shao B, Liang Q, Wang D, He Q, Qina L, Fu Y. Recent advances in conjugated microporous polymers for photocatalysis: designs, applications, and prospects. J Mater Chem A 2020;8:6434–70. https://doi.org/10.1039/D0TA01102A.
[59] Mohamed MG, Elsayed MH, Li CJ, Hassan AE, Mekhemer IMA, Musa AF, Hussien MK, Chen LC, Chen KH, Chou HH, Kuo SW. Reticular design and alkyne bridge engineering in donor–π–acceptor type conjugated microporous polymers for boosting photocatalytic hydrogen evolution. J Mater Chem A 2024;12:7693–710. https://doi.org/10.1039/D3TA07309B.
[60] Xiao J, Xiao Z, Hu J, Gao X, Asim M, Pan L, Shi C, Zhang X, Zou JJ. Rational design of alkynyl-based linear donor− π–acceptor conjugated polymers with accelerated exciton dissociation for photocatalysis. Macromolecules 2022;55:5412–21. https://doi.org/10.1021/acs.macromol.2c00885.
[61] Mohamed MG, Mekhemer IMA, Selim AFH, Katsamitros A, Tasis D, Basit A, Chou HH, Kuo SW. Molecular engineering of donor–acceptor-type conjugated microporous polymers for dual effective photocatalytic production of hydrogen and hydrogen peroxide. Mater Horiz 2025;12:5917–28. https://doi.org/10.1039/D5MH00735F. 12.

[62] Chugh P, Sarma D, Mahat A. Linker engineering in β-Ketoenamine-based covalent organic frameworks for photocatalytic water splitting. J Phys Chem C 2025;129:13194–202. https://doi.org/10.1021/acs.jpcc.5c02456.
[63] Wang LJ, Dong P, Zhang G, Zhang FM. Review and perspectives of β-Keto-enamine-based covalent organic framework for photocatalytic hydrogen evolution. Energy Fuels 2023;37:6323–47. https://doi.org/10.1021/acs.energyfuels.3c00162.
[64] Bai W, Song B, Tian Q, Fu X, Qin A, Tang BZ. Efficient and atom-economic construction of functional β-ketoenamine-linked covalent organic frameworks via amino-Yne click polymerization. Chem Mater 2025;37:5062–71. https://doi.org/10.1021/acs.chemmater.5c00549.
[65] Xiao YZ, Mohammed AAK, Kuo SW, EL-Mahdy AFM. Innovative β-ketoenamine-linked covalent organic frameworks: tailored D1-A-D2-A structure for highly efficient photocatalytic degradation of organic pollutants. Sep Pur Technol 2025;356:129950. https://doi.org/10.1016/j.seppur.2024.129950.
[66] Singh PN, Mohamed MG, Kuo SW. Systematic design and synthesis of conjugated microporous polymers containing pyrene and azobenzene building materials for high-performance energy storage. ACS Appl Energy Mater 2023;6:11342–51. https://doi.org/10.1021/acsaem.3c02252.
[67] Ye W, Wang Y, Li B, Qin, Chen X, Zhang J, Chen M, Zhang C. Design of azo-functionalized D-A conjugated organic polymers for photocatalytic reduction of ultra-low concentration CO_2. Appl Catal B-Env 2025;377:125520. https://doi.org/10.1016/j.apcatb.2025.125520.
[68] Lin Z, Chen J, Duan C, Fan K, Li J, Zou S, Zou F, Yuan L, Zhang Z, Zhang K, Lam MY, Aleksandr SA, Qiu J, Wong KS, Yan H, Yan K. Self-assembly construction of a homojunction of Sn–Pb perovskite using an antioxidant for all-perovskite tandem solar cells with improved efficiency and stability. Energy Env Sci 2024;17:6314–22. https://doi.org/10.1039/D4EE01539H.
[69] Sun G, Shi JW, Mao S, Ma D, He C, Wang H, Cheng Y. Dodecylamine coordinated tri-arm CdS nanorod wrapped in intermittent ZnS shell for greatly improved photocatalytic H_2 evolution. Chem Eng J 2022;429:132382. https://doi.org/10.1016/j.cej.2021.132382.
[70] Li W, Wang Z, Li Y, Ghasemi JB, Li J, Zhang G. Visible-NIR light-responsive 0D/2D CQDs/Sb_2WO_6 nanosheets with enhanced photocatalytic degradation performance of RhB: unveiling the dual roles of CQDs and mechanism study. J Hazard Mater 2022;424:127595. https://doi.org/10.1016/j.jhazmat.2021.127595.
[71] Cheng T, Sun X, Xian T, Yi Z, Li R, Wang X, Yang H. Tert-butylamine/oleic acid-assisted morphology tailoring of hierarchical $Bi_4Ti_3O_{12}$ architectures and their application for photodegradation of simulated dye wastewater. Opt Mater 2021;112:110781. https://doi.org/10.1016/j.optmat.2020.110781.